

Vertical structure of biomass burning aerosol transported over the southeast Atlantic Ocean

Harshvardhan Harshvardhan¹, Richard Ferrare², Sharon Burton², Johnathan Hair², Chris Hostetler², David Harper², Anthony Cook², Marta Fenn³, Amy Jo Scarino³, Eduard Chemyakin³, Detlef Müller⁴

¹Purdue University, West Lafayette, IN, United States

²NASA Langley Research Center, Hampton, VA, United States

³Science Systems and Applications, Inc./NASA Langley Research Center, Hampton, VA, United States

⁴University of Hertfordshire, Hatfield, Hertfordshire, United Kingdom

Correspondence to: H. Harshvardhan (harshvar@purdue.edu)

Abstract. Biomass burning in southwestern Africa produces smoke plumes that are transported over the Atlantic Ocean and overlie vast regions of stratocumulus clouds. This aerosol layer contributes to direct and indirect radiative forcing of the atmosphere in this region, particularly during the months of August, September, and October. There was a multi-year international campaign to study this aerosol and its interactions with clouds. Here we report on the evolution of aerosol distributions and properties as measured by the airborne high spectral resolution lidar (HSRL-2) during the ORACLES (Observations of Aerosols above Clouds and their intEractionS) campaign in September 2016. The NASA Langley HSRL-2 instrument was flown on the NASA ER-2 aircraft for several days in September 2016. Data were aggregated at two pairs of $2^\circ \times 2^\circ$ grid boxes to examine the evolution of the vertical profile of aerosol properties during transport over the ocean. Results showed that the structure of the profile of aerosol extinction and microphysical properties is maintained over a one to two-day time scale. In the 3-5 km altitude range, 95% of the aerosol extinction was contributed by particles in the 0.05-0.50 μm radius size range, with the aerosol in this size range having an average effective radius of 0.16 μm . This indicates that there is essentially no scavenging or dry deposition at these altitudes. Moreover, there is very little day to day variation in these properties, such that time sampling as happens in such campaigns, may be representative of longer periods such as monthly means. Below 3 km there is considerable mixing with larger aerosol, most likely continental source near land. Furthermore, these measurements indicated that there was often a distinct gap between the bottom of the aerosol layer and cloud tops at the selected locations as evidenced by a layer of several hundred meters that contained relatively low aerosol extinction values above the clouds.

1 Introduction

Aerosols are often considered as the most confounding element in the climate system when simulating parameters of the Earth's current climate. Their interaction with clouds makes the problem extremely complicated. The general topic of aerosol-cloud interaction has been of great interest in the scientific community: to quote the report of the Intergovernmental Panel on Climate Change (IPCC AR5) "Clouds and aerosols continue to contribute the largest uncertainty to estimates and interpretations of the Earth's changing energy budget" (Boucher et al., 2013).

35 In the context of these interactions, the interplay of biomass burning (BB) aerosol and the stratocumulus clouds in
36 the Southeast (SE) Atlantic is unique and crucial to the estimates of the energy budget of the region. This BB aerosol
37 arises from the seasonal burning (July-October) of agricultural residue in the southwestern African Savannah and
38 traverses large distances westward over the SE Atlantic Ocean. Unlike the aerosol from industrial activity and biofuels
39 that intermingle with clouds in many regions (Ramanathan et al., 2001; Mechoso et al., 2013), these optically thick
40 BB aerosol layers overlay vast stretches of marine stratus cloud in the SE Atlantic (Chand et al., 2009; Wilcox, 2010;
41 Adebisi et al., 2015) where they have a direct radiative effect. The BB aerosol can also act as nuclei for cloud droplets
42 and so cause a potentially significant cloud albedo effect. Observations and modelling studies of such interactions in
43 the Southeast Atlantic and southern Africa regions include Diamond et al. (2018), Kacarab et al. (2020), Mallet et al.
44 (2020) and Gupta et al. (2022). There is also some evidence that aerosol can alter the thermodynamics of cloud
45 formation through semi-direct effects (Sakaeda et al., 2011). Studies using high resolution limited area models have
46 shown a variety of effects, including stratus to cumulus transition resulting from these interactions (Yamaguchi et al.,
47 2015; Gordon et al., 2018; Lu et al., 2018). The semi-direct effect has also been shown to be important in a limited
48 time run of a global model (Das et al., 2020).

49 During the course of its transport over the Atlantic basin, the dense BB aerosol layer affects the underlying clouds
50 and Earth's radiative balance in multiple ways. It exerts a direct radiative forcing (DRF) by scattering and absorbing
51 solar radiation in the atmosphere; when clouds are present, these aerosols absorb incoming solar radiation along with
52 the radiation reflected by the underlying cloud surface (Chand et al., 2009; Meyer et al., 2013; Zhang et al., 2016).
53 Simultaneously, depending on the relative vertical location of the aerosol with respect to the cloud deck, the cloud
54 cover (fraction) or liquid water path may increase or decrease in response to heating of surrounding air masses due to
55 aerosol absorption and subsequent changes in atmospheric stability, the semi-direct forcing (Sakaeda et al., 2011;
56 Wilcox, 2012; Das et al., 2020). Observations at Ascension Island show that daytime cloud cover and relative humidity
57 are lower when there is more smoke in the marine boundary layer (Zhang and Zuidema, 2019). Moreover, as the
58 marine boundary layer (MBL) deepens farther offshore and north of 5°S, subsiding aerosol particles become entrained
59 into the MBL and interact with the clouds as cloud condensation nuclei to affect their microphysics (indirect forcing)
60 (Costantino and Breon, 2013; Painemal et al., 2014).

61 In the context of simulating the above alluded aerosol radiative effects, it is vital that aerosol-cloud overlap
62 characteristics are accurately represented within the models. The quantification of these aerosol-cloud overlap
63 characteristics in the models is necessary for a variety of reasons. For example, previous studies have found that the
64 sign and magnitude of DRF of absorbing aerosol above clouds (AAC) critically depends upon the reflectance and
65 coverage of the underlying cloud surfaces along with the optical properties, composition and size distribution of the
66 overlying aerosols (Keil and Haywood, 2003; Chand et al., 2009). Additionally, the magnitude and sign of the aerosol
67 semi-direct effects are quite sensitive to the vertical distribution of aerosols, especially with respect to the vertical
68 location of clouds (Penner et al., 2003; McFarquhar and Wang, 2006; Koch and Del Genio, 2010).

69 Here we address the evolution of the vertical properties of BB aerosol as it travels in the marine environment after
70 leaving the African land mass. Section 2 identifies the field campaign and specifies the geographic region selected for
71 the analysis and rationale for that choice. Section 3 describes the attributes of the instrument and key parameters

72 related to the aerosol that can be extracted from the measurements. Section 4 presents the results followed by a
73 summary and conclusion in section 5.

74 **2 Field Campaigns**

75 The concerns mentioned above were the driving force behind plans for several international multi-year field
76 campaigns; ORACLES (Observations of Aerosols above Clouds and their intEractionS, Redemann et al., 2021),
77 CLARIFY-2017 (CLoud-Aerosol-Radiation Interactions and Forcing for Year 2017, Haywood et al., 2021), and
78 LASIC (Layered Atlantic Smoke Interactions with Clouds, Zuidema et al., 2016, 2018). A key component of the
79 September 2016 NASA ORACLES Intensive Observation Period (IOP) was the vertical profiling of aerosol properties
80 measured by an airborne lidar, the NASA Langley High Spectral Resolution Lidar-2, HSRL-2 (Burton et al., 2018),
81 on-board the NASA ER-2, which was based in Walvis Bay, Namibia, for operations during 2016, the deployment
82 covered in this study. In the following two years, the instrument was on-board the P-3 flying out of São Tomé. The
83 siting and flight tracks chosen ensured adequate coverage of the seasonal BB aerosol.

84 **2.1 Meteorology**

85 The September monthly mean meteorological situation is shown in Fig. 1 from MERRA2 reanalysis (Buchard et
86 al., 2017; Randles et al., 2017) along with locations of relevant sites. A thorough meteorological analysis for all
87 ORACLES deployments is provided in Ryoo et al. (2021). For the period under consideration here, they found that
88 the African Easterly Jet-South (AEJ-S), fast moving zonal easterlies centered on 650 hPa around 5-15°S, was active
89 and corresponded closely to the long-term climatology. Fig. 2 shows 650 hPa winds from MERRA2 reanalysis at the
90 beginning, at the end, and on two intermediate days during which HSRL-2 measurements were made. ER-2 flight
91 tracks during the September 2016 IOP are shown in Fig. 3. Note that flights were primarily confined to within roughly
92 1000 km of the African coast with only the 22 September flight venturing further. Flights such as executed during the
93 IOP are unable to follow air parcels in a Lagrangian fashion to examine the evolution of smoke plumes. Here we
94 provide an alternate framework by which to study evolving aerosol properties in an average sense. In order to establish
95 average characteristics of the BB smoke plume as it travels over the ocean, we have chosen five grid boxes of two-
96 degree latitude and longitude on a side at various distances from the source and aggregated observations. The choice
97 of grid boxes was based on the availability of data from the flights (Fig. 3) and the general direction of transport of
98 the smoke as evidenced by the wind fields in Fig. 2. The grid boxes so chosen are marked on Figs. 2 and 3, and the
99 rationale for the choice is explained below.

100 Figure 4 shows 48-hour backward trajectory frequency analyses at 3.5 km, roughly the central altitude of the plume,
101 using NOAA HYSPLIT trajectory calculations (https://www.ready.noaa.gov/HYSPLIT_traj.php) which were carried
102 out using archived GDAS 0.5-degree meteorology (Stein et al., 2015). The frequency distribution is a 48-hour history
103 of the paths taken by air parcels arriving at the grid boxes marked A and C at 3500 m altitude. The time period of the
104 frequency analyses covers the entire period during which HSRL-2 measurements were made, 12-24 September 2016.

105 The selected grid box pairs indicate that Box A receives aerosol that has earlier crossed Box B and Box C is downwind
106 of Box D; boxes B and D receive aerosol directly from BB sources on land. The grid box pairs A/B and C/D can
107 therefore provide information on the evolution of the microphysics and vertical distribution of BB aerosol plumes
108 after leaving the continent. This strategy is similar to that used in comparisons of models with observations for this
109 campaign by Shinozuka et al. (2020), who also showed that observations made on the sampled days were
110 representative of monthly means. In addition to the four boxes strongly influenced by smoke, a southern box, E, has
111 been chosen to provide a control contrast to the other areas in that it is influenced primarily by maritime air as seen
112 from Figs. 1 and 2.

113 **2.2 ORACLES 2016 IOP**

114 The days during the campaign that were included in the averaging procedure are shown in Table 1. Also included
115 is the typical time of the day when the measurements were made, a function of the flight pattern of the ER-2. The
116 number of lidar return profiles averaged for each grid box and statistics related to the backward trajectories are also
117 listed. These grid boxes contained aircraft tracks on multiple days during which trajectory analysis showed near-
118 uniform wind direction between 2.5 and 4.5 km altitude throughout the IOP. With the exception of the grid box
119 centered at 22° S, 9° E, all indicate flow from the source region of BB aerosol. Table 1 also lists the mean and standard
120 deviation of time duration in hours spent over water of air parcels arriving at 3500 m altitude at the grid box during
121 the averaging period. There is no entry for Box E since arriving air had a maritime source and did not originate from
122 land. It must be stressed that the duration is not calculated from the source region on land, which is distributed over a
123 large area of central Africa (e.g., Fig. 9 of Redemann et al., 2021) and cannot be uniquely identified with specific
124 observations made over the ocean. The plume has already been airborne over land for several hours (see Fig. 4) and
125 aerosol would have undergone transformations that occur at short time scales (Cappa et al., 2020). The duration was
126 calculated by running HYSPLIT backward trajectories of air parcels arriving every six hours starting at 0600 UTC on
127 the days of the first flight and ending at 1800 UTC on the days of the last flight of the averaging period and is shown
128 in some detail in Fig. 5, which essentially reflects the profile of the prevailing wind speeds. The inference is that BB
129 smoke at 3500 m altitude arrives at A on average about 30 h after passing B and arrives at C 35 h after passing D. The
130 change in selected aerosol properties as measured by the HSRL-2 during this travel in the marine environment provides
131 information on the evolution of the plume during this time period.

132 **3 HSRL-2**

133 The NASA LaRC HSRL-2 uses the HSRL technique to independently retrieve aerosol extinction and backscatter
134 (Shipley et al., 1983; Grund and Eloranta, 1991; She et al., 1992) without a priori assumptions on aerosol type or
135 extinction-to-backscatter ratio. By using the HSRL technique, HSRL-2, like its predecessor HSRL-1 (Hair et al.,
136 2008), provides accurate backscatter profiles even in situations where the lidar beam is attenuated by overlying cloud
137 or aerosol as long as it is not completely attenuated. The LaRC HSRL-2 employs the HSRL technique at 355 and 532

138 nm, and the standard backscatter technique at 1064 nm. It also measures aerosol and cloud depolarization at all three
139 wavelengths. The HSRL-2 provides vertically resolved measurements of the following extensive and intensive aerosol
140 parameters below the aircraft (approximate archival horizontal, Δx , and vertical resolutions, Δz , are listed assuming
141 ER-2 cruise speed).

142 • *Extensive parameters*¹ – backscatter coefficient, β , at 355, 532, and 1064 nm ($\Delta x \sim 2$ km, $\Delta z \sim 15$ m); extinction
143 coefficient, α , at 355, and 532 nm ($\Delta x \sim 12$ km, $\Delta z \sim 300$ m); optical depth at 355 and 532 nm (integrating the profile
144 of extinction). The aerosol optical depth (AOD) is a critical quantity in discussions of the influence of aerosol on
145 climate (Boucher et al., 2013).

146 • *Intensive parameters* – extinction-to-backscatter ratio of aerosol, the Lidar Ratio, $S_a = \alpha_a / \beta_a$, at 355 and 532 nm
147 ($\Delta x \sim 12$ km, $\Delta z \sim 300$ m); depolarization, $\delta_a = \beta_a^+ / \beta_a^{\parallel}$, at 355, 532, and 1064 nm ($\Delta x \sim 2$ km, $\Delta z \sim 15$ m); and
148 aerosol backscatter wavelength dependence (i.e., Ångström exponent for aerosol backscatter – directly related to the
149 backscatter color ratio) for two wavelength pairs (355-532 and 532-1064 nm, $\Delta x \sim 2$ km, $\Delta z \sim 15$ m).

150 The overall systematic error associated with the backscatter calibration is estimated to be less than 5 % for the 355
151 and 532 nm channels and 20 % for 1064 nm (Burton et al., 2015). Under typical conditions, the total systematic error
152 for extinction is estimated to be less than 0.01 km^{-1} at 532 nm. The random errors for all aerosol products are typically
153 less than 10 % for the backscatter and depolarization ratios (Hair et al., 2008). Rogers et al. (2009) validated the HSRL
154 extinction coefficient profiles and found that the HSRL extinction profiles are within the typical state-of-the-art
155 systematic error at visible wavelengths (Schmid et al., 2006). Since HSRL-2 includes the capability to measure
156 backscatter at three wavelengths and extinction at two wavelengths, “ $3\beta+2\alpha$ ” microphysical retrieval algorithms
157 (Müller et al., 1999a, 1999b; Veselovskii et al., 2002) are used to retrieve height-resolved parameters such as aerosol
158 effective radius and number, surface, and volume concentrations (Müller et al., 2014, Sawamura et al., 2016). Here
159 we restrict ourselves to the effective radius of the particles.

160 4 Results

161 In this study of the vertically resolved evolving properties of BB aerosol, we present key lidar measurements and
162 microphysical results obtained by performing the “ $3\beta+2\alpha$ ” retrieval mentioned in Section 3.

163
164

¹ By the term *extensive*, we refer to optical parameters, such as extinction, that are influenced by the amount (concentration) and type (size, composition, shape) of aerosol/cloud particles. *Intensive* properties, on the other hand, are those that depend only on the nature of the particles and not on their quantity or concentration, but rather depend only on aerosol type (Anderson et al., 2003).

165 4.1 Lidar

166 Vertical profiles averaged over the times of overflight in $2^\circ \times 2^\circ$ latitude/longitude boxes shown in Figure 3 on the
167 days given in Table 1 are for the following properties.

- 168 1. Aerosol Extinction at 532 nm, α_a , determined by aerosol number concentration, microphysical
169 properties and relative humidity
- 170 2. Backscatter Ångström exponent between 1064 and 532 nm, an indication of particle size.
- 171 3. Aerosol Depolarization at 532 nm, a measure of particle asphericity.
- 172 4. Aerosol extinction to backscatter ratio, the Lidar Ratio, at 532 nm, a marker for aerosol composition.

173 Inspection of the wind field at 650 hPa in Fig. 2 and backward trajectory frequency plots in Fig. 4 suggest that the
174 grid boxes chosen fit naturally into two pairs of tracks of the widespread BB aerosol field. The northern pair, identified
175 in Table 1 as A and B, centered around 10° S, are in a faster zonal track, whereas the grid boxes C and D are in a track
176 centered between $13\text{-}15^\circ$ S that is slightly slower and has a component from the north over a stretch of water (Fig. 2).
177 The two pairs can then provide information on the evolution of aerosol properties over a time scale of one to two days.
178 Figures 6-9 show the aerosol extinction, backscatter Ångström exponent, aerosol depolarization and Lidar Ratio for
179 the two pairs of grid boxes and Box E, which is at the southern edge of the region influenced by the BB aerosol. The
180 results presented are one-minute averages of independent 10 s vertical profiles for backscatter Ångström exponent
181 and depolarization and one-minute averages for extinction and lidar ratio profiles. From Table 1, the mean time elapsed
182 between B and A is 29.4 h and that between D and C is 34.9 h. It should be pointed out that parameter values shown
183 below the level of mean cloud top are averages of lidar returns through breaks in the stratus deck and are not relevant
184 for this study. If we use the low cut-off of an extinction coefficient of 15 Mm^{-1} to indicate an aerosol-free layer
185 (Shinozuka et al., 2020), then Fig. 6 indicates that the bulk of the smoke layers encountered at these distances from
186 land were separated from the cloud top, a feature more prevalent during the 2016 IOP than in 2017 and 2018
187 (Redemann et al., 2021).

188 The northern plume is a column of aerosol of relatively constant extinction from just above 2.5 km to 5 km while
189 the southern plume has a profile of extinction that increases nearly linearly with height from a minimum near the cloud
190 top to a maximum at 5 km (Fig. 6). The vertical structure of the aerosol profiles measured by HSRL-2 was compared
191 to water vapor profiles represented by the Modern-Era Retrospective analysis for Research and Applications, Version
192 2 (MERRA2) model. Pistone et al. (2021) explored the relationship between aerosols, CO, water vapor as measured
193 by ORACLES airborne in situ measurements and represented by models including MERRA2. They found the
194 MERRA2 water vapor profiles, like the measured water vapor profiles, exhibited a linear relationship with CO and
195 biomass burning plume strength; they also found that smoky, humid air produced by daytime convection over the
196 continent advected over the ocean and into the ORACLES study region. MERRA2 water vapor profiles produced at
197 three hourly increments and 72 pressure levels were interpolated to the times and locations of the HSRL-2 profiles.
198 Water vapor mixing ratio generally decreased significantly just above the PBL then increased for altitudes around 2
199 to 3 km before decreasing again. This behavior is generally consistent with the relationship between water vapor and
200 aerosol scattering reported by Pistone et al. (2021).

201 Figure 10 shows the median, 25th and 75th percentile relative humidity (RH) profiles computed by interpolating the
202 MERRA2 0.5-deg. 3-hourly humidity profiles to the locations and times of the HSRL-2 measurements. The profiles
203 typically show a more pronounced increase in RH with altitude that more closely follows the HSRL-2 measurements
204 of aerosol extinction profiles, although the MERRA2 profiles typically begin decreasing above 4 km whereas the
205 airborne in situ RH measurements and HSRL-2 aerosol extinction profiles begin decreasing above 5 km. Interestingly,
206 during three of the dates (Sept. 12, 16, 22) considerable portions of the smoke layers correspond to MERRA2 relative
207 humidity above 60-70%. This increase in RH with altitude could help explain at least some of the increase in aerosol
208 extinction with height observed in the HSRL-2 profiles of the C/D Box pair. Aerosol humidification often amplified
209 the increase in aerosol extinction by factors of 1.5 or more (Doherty et al., 2022).

210 The Ångström exponent (Fig. 7) and depolarization (Fig. 8) indicate the presence of fine spherical particles at the
211 top of the plume and increasing sizes towards the bottom. The Lidar Ratio (Fig. 9) above 3 km for the two pairs is
212 between 70 and 80 sr, suggesting strong absorption (Müller et al., 2019) but is considerably less and highly variable
213 in Box E and in the lower layers of the aerosol plume in Box D, where the smoke plume most likely has components
214 of continental aerosol such as dust and pollution typical of the nearby Namibian coast (Klopper et al., 2020). The most
215 striking feature of the results is the very small profile-to-profile variability of the intensive lidar parameters in the
216 upper two kilometers of the plume over the course of several days as evident from the range of values in the 25-75
217 percentile shaded grey in Figs. 7-9. This suggests strongly that the particles maintain their size, shape and absorbing
218 properties over the first few days of transport over the ocean. This result is of some importance for climate studies in
219 which the radiative properties of BB aerosol are input to the calculation of radiative forcing. Complex chain aggregates
220 as found near the source of fires (Pósfai et al., 2003, China et al., 2013) are typically not represented in climate models.
221 However, if the aerosol is already spherical and maintains its size over the time period of radiative interactions being
222 studied, then core-shell models of varying degrees of complexity could perhaps suffice (Zhang et al., 2020). The lower
223 portion of the plume containing larger BB aerosol particles is subject to mixing with marine and continental particles
224 from regions not affected by biomass burning and is highly variable in nature. This would be more difficult to model
225 but Fig. 6 shows that the aerosol extinction coefficient decreases rapidly at lower levels so errors in representation
226 may be acceptable.

227 4.2 Microphysics

228 The lidar measurements are inverted to obtain information regarding particle size. The inversion is performed on one-
229 minute averages of six independent 10 s backscatter profiles and one-minute average extinction profiles. Details of
230 the inversion process are in Müller et al. (2019) and references therein. The particle size distribution is represented
231 using a series of eight triangular basis functions that can represent both monomodal and bimodal size distributions
232 (*ibid*). Points to note are that the procedure makes the following assumptions: the particles are spherical and
233 homogeneous having wavelength-independent complex index of refraction. The low (< 5 %) values of depolarization
234 through most of the plume, shown in Fig. 8, suggests that the spherical assumption is justified. There is most likely
235 structure and inhomogeneity in the core of the particles, but current particle optical models are unable to incorporate

236 these complexities. Results from this inversion procedure have been compared to coincident airborne in situ particle
237 measurements. Müller et al. (2014) present results from a campaign off the northeast coast of the US showing that the
238 inversion results agree with in situ measurements of effective radius and also number, surface area and volume
239 concentration within error bars. Sawamura et al. (2017) report on campaigns in the wintertime San Joaquin Valley of
240 California and summertime near Houston, TX. They found high correlation and low bias in surface and volume
241 concentration in situ measurements relative to HSRL with the best agreement for submicron fine-mode aerosol, which
242 is most relevant to the current study. Müller et al. (2019) report retrievals and their uncertainty for one day in the
243 ORACLES campaign, 22 September 2016. Considering only optical data with strong signal-to-noise ratio, they
244 estimate retrieval errors are 25 % for number concentration. The relative uncertainty in effective radius for parts of
245 the flight track where particle size was nearly constant was below 20 %.

246 In order to help separate particles that have BB source from coarser particles of continental or marine origin, we
247 specify a Submicron Fraction (SMF) as the contribution to the extinction at 532 nm of particles in the radius range
248 0.05-0.50 μm (Anderson et al., 2005). Figure 11 shows the profiles of SMF for the five grid boxes and not surprisingly,
249 the bulk of the smoke plume, especially between 3 and 5 km contains aerosol almost entirely in the submicron range.
250 Below 3 km, at locations both near and further way from the coast, there is a marked increase in the fraction of larger
251 particles. The increase in depolarization (Fig. 8) at these lower levels and a decrease in the Lidar Ratio (Fig. 9) suggest
252 mixing with the aforementioned non-BB aerosol particles. However, the sharp decrease in extinction below 3 km (Fig.
253 6) indicates that their contribution to direct radiative effects would be minimal. Finally, Fig. 12 shows the vertical
254 profile of the effective radius of the SMF aerosol population. The effective radius is 0.16 μm with little variation
255 between 3 and 5 km. Of greater significance is that it remains very similar between the pairs of grid boxes along the
256 transport trajectory of the smoke. The retrieved effective radius is similar to the results presented by Müller et al.
257 (2014) for a mixture of urban aerosol and smoke. Their comparison with in situ measurements showed a slight
258 overestimate but within a standard deviation. The retrieved and in situ results also show that the particle size is uniform
259 with altitude even when the number concentration drops by a factor of three. Another set of prior comparisons of
260 HSRL-2 and in situ measurements is provided in Sawamura et al. (2017). Here again, the effective radius of the
261 submicron fraction of particles, 0.15 μm , is uniform with altitude, and comparable though biased slightly low
262 compared to in situ observations.

263 The effective radii of the SMF aerosols, which typically vary between 0.15 to 0.20 μm , are generally consistent
264 with the sizes reported previously for smoke aerosol in the ORACLES region. Haywood et al. (2021) provide a
265 composite of the aerosol sizes for biomass burning aerosol off the South African coast. These size distributions, which
266 were derived from airborne in situ measurements (Haywood et al., 2003; Peers et al., 2019; Wu et al., 2020), typically
267 correspond to SMF aerosol effective radii between 0.14-0.17 μm and were for the dry aerosol. Shinozuka et al. (2020)
268 reported on airborne aerosol sizes measured during ORACLES by an Ultra-High-Sensitivity-Aerosol Spectrometer
269 (UHSAS) deployed on the NASA P-3 aircraft. The UHSAS measured particles with dry diameters between 60 and
270 1000 nm. SMF aerosol effective radii derived from the UHSAS measurements of volume mean diameter were
271 generally around 0.09-0.10 μm for the dry aerosol. Shinozuka et al. (2020) noted that the UHSAS measurements were
272 somewhat undersized and so were adjusted to account for this effect; this adjustment improved scattering closure with

273 coincident nephelometer measurements. As discussed in section 4.1, the RH on some days was above 60-70% so that
274 effective radii under ambient conditions could be expected to be somewhat higher than for the dry aerosol. Using
275 measurements from an airborne Differential Aerosol Sizing and Hygroscopicity Spectrometer Probe (DASH-SP),
276 Shingler et al. (2016) quantified the size-resolved growth factors for several aerosol types; they found that at RH~70-
277 80%, particle diameters for biomass burning aerosols were about 15-20% larger than for the dry aerosol. Xu et al.
278 (2021) derived aerosol properties during the 2016 ORACLES mission using an inversion algorithm that combined
279 HSRL-2 and Research Scanning Polarimeter (RSP) remote sensing measurements. These retrieved aerosol properties
280 were then compared with those derived from the UHSAS measurements described by Shinozuka et al. (2020). For
281 measurements acquired on Sept. 12, 2016, the SMF aerosol effective radius derived from the remote sensing
282 measurements were generally between 0.12-0.15 μm and were only slightly (0.012 μm) higher than the effective radii
283 for the (dry) SMF aerosol derived from the UHSAS measurements. This suggests that some of this difference is
284 associated with differences in RH between the remote sensing retrievals and the in situ measurements.

285 5 Conclusions

286 The results of the aggregated HSRL-2 profiles during the 2016 ORACLES IOP presented here show two main
287 findings. These are however limited to a brief period in the transport of BB smoke from continental Africa over marine
288 clouds in the Atlantic Ocean. This is a limitation of the 2016 campaign because the flight tracks remained within 1000
289 km of the coast. For the period of one to two days after crossing the land-ocean boundary, the fraction of all particles
290 that are in the submicron range in the main smoke plume between 3 and 5 km is around 95 %. The effective radius of
291 the submicron particles in this altitude interval is 0.16 μm and essentially constant with altitude. The particle size is
292 comparable to measured particle sizes in previous campaigns that sampled aerosol that was a mixture of urban haze
293 and smoke (Müller et al., 2014; Sawamura et al., 2017). Moreover, the shape of the median vertical profile of
294 extinction does not change during the first two days of transport over water suggesting the absence of dry deposition
295 and wet scavenging. The low (< 0.05) depolarization ratio of the submicron particles signifies that they are well coated
296 and the assumption of sphericity in the inversion procedure and models that estimate the radiative effects of aerosol
297 is justified. The BB aerosol mix with continental and marine aerosol at the base of the plume but during the September
298 2016 IOP this layer of mixed aerosol tended to have very low extinction coefficients suggesting low abundance and
299 there was often a distinct gap between the plume and the cloud tops.

300 The HSRL-2 instrument was also deployed in the 2017 and 2018 ORACLES campaigns but was deployed on the
301 NASA P-3 which often flew at low altitude to acquire in situ measurements of aerosols and clouds. Consequently, the
302 HSRL-2 was not able to make continuous measurements of the BB aerosol plumes in a manner similar as when
303 deployed on the ER-2. However, there are segments of the track that can provide similar information to the data
304 obtained in the 2016 campaign but for a different time period. Moreover, some flight tracks extended much further
305 from land (Doherty et al., 2021). Analysis of the later campaigns will provide information on the physical evolution
306 of aerosol that has aged for a longer period than is covered in this study.

307 **Data Management**

308 HSRL-2 optical data and retrieved inversion data are available at the NASA archive site
309 <https://espoarchive.nasa.gov/archive/browse/oracles/id8/ER2> and are permanently archived at
310 doi:10.5067/SUBORBITAL/ORACLES/ER2/2016_V1.

311 **Acknowledgements**

312 The lead author would like to thank NASA Langley Research Center for hosting him during a sabbatical when this
313 study was initiated. HSRL-2 participation in ORACLES was supported by NASA through the Earth Venture
314 Suborbital-2 (EVS-2) program (grant no. 13-EVS2-13-0028). Funding for this work was also provided by NASA
315 through the Radiation Sciences Program. We wish to thank the NASA ER-2 pilots and ground crew for their extensive
316 support during ORACLES.

317

- 319 Anderson, T. L., Charlson, R. J., Winker, D. M., Ogren, J. A., and Holmén, K.: Mesoscale variations of tropospheric
320 aerosols, *J. Atmos. Sci.*, 60(1), 119-136, 2003.
- 321 Anderson, T. L., Wu, Y., Chu, D. A., Schmid, B., Redemann, J., and Dubovik, O.: Testing the MODIS satellite
322 retrieval of aerosol fine-mode fraction, *J. Geophys. Res.*, 110, D18204, doi:10.1029/2005JD005978, 2005.
- 323 Adebisi, A. A., Zuidema, P., Chang, I., Burton, S. P., and Cairns, B.: Mid-level clouds are frequent above the Southeast
324 Atlantic stratocumulus clouds, *Atmos. Chem. Phys.*, 20, 11025-11043, doi:10.5194/acp-20-11025-2020, 2020.
- 325 Boucher, O., Randall, D., Artaxo, P., Bretherton, C., Feingold, G., Forster, P., Kerminen, V.-M., Kondo, Y., Liao, H.,
326 Lohmann, U., Rasch, P., Satheesh, S. K., Sherwood, S., Stevens, B., and Zhang X.Y.: Clouds and Aerosols. In:
327 *Climate Change 2013: The Physical Science Basis. Contribution of Working Group I to the Fifth Assessment Report*
328 *of the Intergovernmental Panel on Climate Change [Stocker, T. F., Qin, D., Plattner, G.-K., Tignor, M., Allen, S.*
329 *K., Boschung, J., Nauels, A., Xia, Y., Bex V., and Midgley, P. M. (eds.)]. Cambridge University Press, 2013.*
- 330 Buchard, V., Randles, C. A., da Silva, A. M., Darmenov, A., Colarco, P. R., Govindaraju, R., Ferrare, R. A., Hair, J.,
331 Beyersdorf, A. J., Ziemba L. D., and Yu, H.: The MERRA-2 aerosol reanalysis, 1980 onwards Part II: Evaluation
332 and case studies, *J. Climate*, 30, 6851-6871, doi:10.1175/JCLI-D-16-0613.1, 2017.
- 333 Burton, S. P., Hostetler, C. A., Cook, A. L., Hair, J. W., Seaman, S., Scola, S., Harper, D. B., Smith, J. A., Fenn, M
334 A., Ferrare, R. A., Saide, P. E., Chemyakin, E. V., and Müller, D.: Calibration of a high spectral resolution lidar
335 using a Michelson interferometer with data examples from ORACLES, *Appl. Optics*, 57, 6061-6075, 2018.
- 336 Burton, S. P., Hair, J. W., Kahnert, M., Ferrare, R. A., Hostetler, C. A., Cook, A. L., Harper, D. B., Berkoff, T. A.,
337 Seaman, S. T., Collins, J. E., Fenn, M. A., and Rogers, R. R.: Observations of the spectral dependence of linear
338 particle depolarization ratio of aerosols using NASA Langley airborne High Spectral Resolution Lidar, *Atmos.*
339 *Chem. Phys.*, 15, 13453–13473, doi.org/10.5194/acp-15-13453-2015, 2015.
- 340 Cappa, C. D., Lim, C. Y., Hagan, D. H., Coggon, M., Koss, A., Sekimoto, K., de Gouw, J., Onasch, T. B., Warneke,
341 C., and Kroll, J. H.: Biomass-burning-derived particles from a wide variety of fuels – Part 2: Effects of
342 photochemical aging on particle optical and chemical properties, *Atmos. Chem. Phys.*, 20, 8511-8532,
343 doi:10.5194/acp-20-8511-2020, 2020.
- 344 Chand, D., Wood, R., Anderson, T. L., Satheesh, S. K., and Charlson, R. J.: Satellite-derived direct radiative effect of
345 aerosols dependent on cloud cover, *Nat. Geosci.*, 2, 181-184, doi:10.1038/Ngeo437, 2009.
- 346 China, S., Mazzoleni, C., Gorkowski, K., Aiken, A. C., and Dubey, M. K.: Morphology and mixing state of individual
347 freshly emitted wildfire carbonaceous particles, *Nat. Commun.*, 4:2122 doi: 10.1038/ncomms3122, 2013.
- 348 Costantino, L., and Bréon F. M.: Aerosol indirect effect on warm clouds over South-East Atlantic from co-located
349 MODIS and CALIPSO observations, *Atmos. Chem. Phys.*, 13, 69-88, doi:10.5194/acp-13-69-2013, 2013.
- 350 Das, S., Harshvardhan, H., and Colarco, P. R.: The influence of elevated smoke layers on stratocumulus clouds over
351 the SE Atlantic in the NASA Goddard Earth Observing System (GEOS) Model, *J. Geophys. Res. Atmos.*, 125,
352 e2019JD031209. doi:10.1029/2019JD031209, 2020.
- 353 Diamond, M. S., Dobracki, A., Freitag, S., Small Griswold, J. D., Heikkila, A., Howell, S. G., Kacarab, M. E.,
354 Podolske, J. R., Saide, P. E., and Wood, R.: Time-dependent entrainment of smoke presents an observational
355 challenge for assessing aerosol–cloud interactions over the southeast Atlantic Ocean, *Atmos. Chem. Phys.*, 18,
356 14623–14636, <https://doi.org/10.5194/acp-18-14623-2018>, 2018.
- 357 Doherty, S. J., Saide, P. E., Zuidema, P., Shinzuka, Y., Ferrada, G. A., Gordon, H., Mallet, M., Meyer, K.,
358 Painemal, D., Howell, S. G., Freitag, S., Dobracki, A., Podolske, J. R., Burton, S. P., Ferrare, R. A., Howes, C.,
359 Nabat, P., Carmichael, G. R., da Silva, A., Pistone, K., Chang, I., Gao, L., Wood, R., and Redemann, J.: Modeled
360 and observed properties related to the direct aerosol radiative effect of biomass burning aerosol over the Southeast
361 Atlantic, *Atmos. Chem. Phys.*, 22, 1-46, <https://doi.org/10.5194/acp-22-1-2022>, 2022.
- 362 Gordon, H., Field, P. R., Abe, S. J., Dalvi, M., Grosvenor, D. P., Hill, A. A., Johnson, B. T., Miltenberger, A. K.,
363 Yoshioka, M., and Carslaw, K. S.: Large simulated radiative effects of smoke in the south-east Atlantic, *Atmos.*
364 *Chem. Phys.*, 18, 15261-15289, doi:10.5194/acp-18-15261-2018, 2018.
- 365 Grund, C. J., and Eloranta, E. W.: University of Wisconsin high spectral resolution lidar, *Opt. Eng.*, 30, 6-12, 1991.
- 366 Gupta, S., McFarquhar, G. M., O'Brien, J. R., Poellot, M. R., Delene, D. J., Miller, R. M., and Small Griswold, J. D.:
367 Factors affecting precipitation formation and precipitation susceptibility of marine stratocumulus with variable
368 above- and below-cloud aerosol concentrations over the Southeast Atlantic, *Atmos. Chem. Phys.*, 22, 2769-2793,
369 <https://doi.org/10.5194/acp-22-2769-2022>, 2022.
- 370 Hair, J. W., Hostetler, C. A., Cook, A. L., Harper, D. B., Ferrare, R. A., Mack, T. L., Welch, W., Izquierdo, L. R.,
371 Hovis, F. E.: Airborne High Spectral Resolution Lidar for profiling aerosol optical properties, *Appl. Optics*, 47, doi:
372 10.1364/AO.47.006734, 2008.

373 Haywood, J. M., Osborne, S. R., Francis, P. N., Keil, A., Formenti, P., Andreae, M. O., and Kaye, P. H.: The mean
374 physical and optical properties of regional haze dominated by biomass burning aerosol measured from the C-130
375 aircraft during SAFARI 2000, *J. Geophys. Res.*, 108, 8473, <https://doi.org/10.1029/2002JD002226>, 2003.

376 Haywood, J. M., Abel, S. J., Barrett, P. A., Bellouin, N., Blyth, A., Bower, K. N., Brooks, M., Carslaw, K., Che, H.,
377 Coe, H., Cotterell, M. I., Crawford, I., Cui, Z., Davies, N., Dingley, B., Field, P., Formenti, P., Gordon, H., de
378 Graaf, M., Herbert, R., Johnson, B., Jones, A. C., Langridge, J. M., Malavelle, F., Partridge, D. G., Peers, F.,
379 Redemann, J., Stier, P., Szpek, K., Taylor, J. W., Watson-Parris, D., Wood, R., Wu, H., and Zuidema, P.: The
380 CLOUD–Aerosol–Radiation Interaction and Forcing: Year 2017 (CLARIFY-2017) measurement campaign, *Atmos.*
381 *Chem. Phys.*, 21, 1049–1084, <https://doi.org/10.5194/acp-21-1049-2021>, 2021.

382 Kacarab, M., Thornhill, K. L., Dobracki, A., Howell, S. G., O'Brien, J. R., Freitag, S., Poellot, M. R., Wood, R.,
383 Zuidema, P., Redemann, J., and Nenes, A.: Biomass burning aerosol as a modulator of the droplet number in the
384 southeast Atlantic region, *Atmos. Chem. Phys.*, 20, 3029–3040, <https://doi.org/10.5194/acp-20-3029-2020>, 2020.

385 Keil, A., and Haywood, J. M.: Solar radiative forcing by biomass burning aerosol particles during SAFARI 2000: A
386 case study based on measured aerosol and cloud properties, *J. Geophys. Res. Atmos.*, 108, 8467,
387 doi:10.1029/2002JD002315, 2003.

388 Klopper, D., Formenti, P., Namwoonde, A., Cazaunau, M., Chevaillier, S., Feron, A., Gaimoz, C., Hease, P., Lahmidi,
389 F., Mirande-Bret, C., Triquet, S., Zeng, Z., and Piketh, S. J.: Chemical composition and source apportionment of
390 atmospheric aerosols on the Namibian coast, *Atmos. Chem. Phys.*, 20, 15,811–15,833, doi:10.5194/acp-20-15811-
391 2020, 2020.

392 Koch, D., and Del Genio A. D.: Black carbon semi-direct effects on cloud cover: review and synthesis, *Atmos. Chem.*
393 *Phys.*, 10, 7685–7696, doi:10.5194/acp-10-7685-2010, 2010.

394 Lu, Z., Liu, X., Zhang, Z., Zhao, C., Meyer, K., Rajapakshe, C., Wu, C., Yang, Z., and Penner, J.: Biomass smoke
395 from southern Africa can significantly enhance the brightness of stratocumulus over the southeastern Atlantic
396 Ocean, *Proc. Natl. Acad. Sci.*, 115, 2924–2929, doi:10.1073/pnas.1713703115, 2018.

397 Mallet, M., Solmon, F., Nabat, P., Elguindi, N., Waquet, F., Bouniol, D., Sayer, A. M., Meyer, K., Roehrig, R.,
398 Michou, M., Zuidema, P., Flaant, C., Redemann, J., and Formenti, P.: Direct and semi-direct radiative forcing of
399 biomass-burning aerosols over the southeast Atlantic (SEA) and its sensitivity to absorbing properties: a regional
400 climate modeling study, *Atmos. Chem. Phys.*, 20, 13191–13216, <https://doi.org/10.5194/acp-20-13191-2020>, 2020.

401 McFarquhar, G. M., and Wang, H.: Effects of aerosols on trade wind cumuli over the Indian Ocean: Model
402 simulations, *Q. J. R. Meteorol. Soc.*, 132, 821–843, doi: 10.1256/qj.04.179, 2006.

403 Mechoso, C. R., Wood, R., Weller, R., Bretherton, C. S., Clarke, A. D., Coe, H., Fairall, C., Farrar, J. T., Feingold,
404 G., Garreaud, R., Grados, C., McWilliams, J., de Szoeke, S. P., Yuter, S. E., and Zuidema, Z.: Ocean–cloud–
405 atmosphere–land interactions in the Southeastern Pacific: The VOCALS program, *B. Am. Meteorol. Soc.*, 95, 357-
406 375, doi:10.1175/BAMS-D-11-00246.1, 2013.

407 Meyer, K., Platnick, S., Oreopoulos, L., and Lee, D.: Estimating the direct radiative effect of absorbing aerosols
408 overlying marine boundary layer clouds in the southeast Atlantic using MODIS and CALIOP, *J. Geophys. Res.*
409 *Atmos.*, 118, 4801–4815, doi:10.1002/jgrd.50449, 2013.

410 Müller, D., Wandinger, U., and Ansmann, A.: Microphysical particle parameters from extinction and backscatter lidar
411 data by inversion with regularization: theory, *Appl. Optics*, 38, 2346–2357, 1999a.

412 Müller, D., Wandinger, U., and Ansmann, A.: Microphysical particle parameters from extinction and backscatter lidar
413 data by inversion with regularization: simulation, *Appl. Optics*, 38, 2358–2368, 1999b.

414 Müller, D., Hostetler, C. A., Ferrare, R. A., Burton, S. P., Chemyakin, E., Kolgotin, A., Hair, J. W., Cook, A. L.,
415 Harper, D. B., Rogers, R. R., Hare, R. W., Cleckner, C. S., Obland, M. D., Tomlinson, J., Berg, L. K., and Schmid,
416 B.: Airborne multiwavelength high spectral resolution lidar (HSRL-2) observations during TCAP 2012: vertical
417 profiles of optical and microphysical properties of a smoke/urban haze plume over the northeastern coast of the US,
418 *Atmos. Meas. Tech.*, 7, 3487–3496, doi:10.5194/amt-7-3487-2014, 2014.

419 Müller, D., Chemyakin, E., Kolgotin, A., Ferrare, R. A., Hostetler, C. A., and Romanov, A.: Automated, unsupervised,
420 inversion of multiwavelength lidar data with TiARA: assessment of retrieval performance of microphysical
421 parameters using simulated data, *Appl. Optics*, 58, 4981–5007, doi:10.1364/AO.58.004981, 2019.

422 Painemal, D., Kato, S., and Minnis, P.: Boundary layer regulation in the southeast Atlantic cloud microphysics during
423 the biomass burning season as seen by the A-train satellite constellation, *J. Geophys. Res. Atmospheres*, 119,
424 11,288–211,302, doi:10.1002/2014JD022182, 2014.

425 Peers, F., Francis, P., Fox, C., Abel, S. J., Szpek, K., Cotterell, M. I., Davies, N. W., Langridge, J. M., Meyer, K. G.,
426 Platnick, S. E., and Haywood, J. M.: Observation of absorbing aerosols above clouds over the south-east Atlantic
427 Ocean from the geostationary satellite SEVIRI – Part 1: Method description and sensitivity, *Atmos. Chem. Phys.*,
428 19, 9595–9611, <https://doi.org/10.5194/acp-19-9595-2019>, 2019.

429 Penner, J. E., Zhang, S. Y., and Chuang, C. C.: Soot and smoke aerosol may not warm climate, *J. Geophys. Res.*
430 *Atmospheres*, 108, 4657, doi:10.1029/2003JD003409, 2003.

431 Pistone, K., Zuidema, P., Wood, R., Diamind, M., da Silva, A. M., Ferrada, G., Saide, P. E., Ueyama, R., Ryoo, J.-
432 M., Pfister, L., Podolske, J., Noone, D., Bennett, R., Stith, E., Carmichael, G., Redemann, J., Flynn, C., LeBlanc,
433 S., Segal-Rozenhaimer, M., and Shinozuka, Y.: Exploring the elevated water vapor signal associated with the free
434 tropospheric biomass burning plume over the southeast Atlantic Ocean, *Atmos. Chem. Phys.*, 21, 9643-9668,
435 <https://doi.org/10.5194/acp-21-9643-2021>, 2021.

436 Pósfai, M., Simonics, R., Li, J., Hobbs, P. V., and Buseck, P. R.: Individual aerosol particles from biomass burning in
437 southern Africa: 1. Compositions and size distributions of carbonaceous particles, *J. Geophys. Res.*, 108, 8483,
438 doi:10.1029/2002JD002291, 2003.

439 Ramanathan, V., Crutzen, P. J., Kiehl, J. T., and Rosenfeld, D.: Aerosols, climate, and the hydrological cycle, *Science*,
440 294(5549), 2119-2124, doi:10.1126/science.1064034, 2001.

441 Randles, C.A., daSilva, A. M., Buchard, V., Colarco, P. R., Darmenov, A., Govindaraju, P., Smirnov, A., Holben, B.,
442 Ferrare, R. A., Hair, J., Shinozuka, Y., and Flynn, C. J.: The MERRA-2 aerosol reanalysis, 1980 onward. Part I:
443 System description and data assimilation evaluation, *J. Climate*, 30, 6823–6850, doi: 10.1175/JCLI-D-16-0609.1,
444 2017.

445 Redemann, J., Wood, R., Zuidema, P., Doherty, S. J., Luna, B., LeBlanc, S. E., Diamond, M. S., Shinozuka, Y., Chang,
446 I. Y., Ueyama, R., Pfister, L., Ryoo, J.-M., Dobracki, A. N., da Silva, A. M., Longo, K. M., Kacenelenbogen, M.
447 S., Flynn, C. J., Pistone, K., Knox, N. M., Piketh, S. J., Haywood, J. M., Formenti, P., Mallet, M., Stier, P.,
448 Ackerman, A. S., Bauer, S. E., Fridlind, A. M., Carmichael, G. R., Saide, P. E., Ferrada, G. A., Howell, S. G.,
449 Freitag, S., Cairns, B., Holben, B. N., Knobelspiesse, K. D., Tanelli, S., L'Ecuyer, T. S., Dzambo, A. M., Sy, O. O.,
450 McFarquhar, G. M., Poellot, M. R., Gupta, S., O'Brien, J. R., Nenes, A., Kacarab, M., Wong, J. P. S., Small-
451 Griswold, J. D., Thornhill, K. L., Noone, D., Podolske, J. R., Schmidt, K. S., Pilewskie, P., Chen, H., Cochrane, S.
452 P., Sedlacek, A. J., Lang, T. J., Stith, E., Segal-Rozenhaimer, M., Ferrare, R. A., Burton, S. P., Hostetler, C. A.,
453 Diner, D. J., Seidel, F. C., Platnick, S. E., Myers, J. S., Meyer, K. G., Spangenberg, D. A., Maring, H., and Guo, L.:
454 An overview of the ORACLES (ObseRvations of Aerosols above Clouds and their intEractionS) project: aerosol-
455 cloud-radiation interactions in the southeast Atlantic basin, *Atmos. Chem. Phys.*, 21, 1507-1563, doi:10.5194/acp-
456 21-1507-2021, 2021.

457 Rogers, R. R., Hair, J. W., Hostetler, C. A., Ferrare, R. A., Obland, M. D., Cook, A. L., Harper, D. B., Burton, S. P.,
458 Shinozuka, Y., McNaughton, C. S., Clarke, A. D., Redemann, J., Russell, P. B., Livingston, J. M., and Kleinman,
459 L. I.: NASA LaRC airborne high spectral resolution lidar aerosol measurements during MILAGRO: observations
460 and validation, *Atmos. Chem. Phys.*, 9, 4811-4826, 2009.

461 Ryoo, J.-M., Pfister, L., Ueyama, R., Zuidema, P., Wood, R., Chang, I., and Redemann, J.: A meteorological
462 overview of the ORACLES (ObseRvations of Aerosols above CLouds and their intEractionS) campaign over the
463 southeastern Atlantic during 2016–2018: Part 1 – Climatology, *Atmos. Chem. Phys.*, 21, 16689–16707,
464 <https://doi.org/10.5194/acp-21-16689-2021>, 2021.

465 Sakaeda, N., Wood, R., and Rasch, P. J.: Direct and semidirect aerosol effects of southern African biomass burning
466 aerosol, *J. Geophys. Res. Atmospheres*, 116, D12205, doi:10.1029/2010JD015540, 2011.

467 Sawamura, P., Moore, R. H., Burton, S. P., Chemyakin, E., Müller, D., Kolgotin, A., Ferrare, R. A., Hostetler, C. A.,
468 Ziemba, L. D., Beyersdorf, A. J., and Anderson, B. E.: HSRL-2 aerosol optical measurements and microphysical
469 retrievals vs. airborne in situ measurements during DISCOVER-AQ 2013: an intercomparison study, *Atmos. Chem.*
470 *Phys.*, 17, 7229-7243, doi.org/10.5194/acp-17-7229-2017, 2017.

471 Schmid, B., Ferrare, R. A., Flynn, C., Elleman, R., Covert, D., Strawa, A., Welton, E., Turner, D., Jonsson, H.,
472 Redemann, J., Eilers, J., Ricci, K., Hallar, A. G., Clayton, M., Michalsky, J., Smirnov, A., Holben, B., and Barnard,
473 J. : How well do state-of-the-art techniques measuring the vertical profile of tropospheric aerosol extinction
474 compare? *J. Geophys. Res.*, 111, D05S07, doi:10.1029/2005JD005837, 2006.

475 She, C. Y., Alvarez II, R. J., Caldwell, L. M., and Krueger, D. A.: High-spectral-resolution Rayleigh-Mie lidar
476 measurement of aerosol and atmospheric profiles, *Opt. Lett.*, 17, 541-543, 1992.

477 Shingler, T., Crosbie, E., Ortega, A., Shiraiwa, M., Zuend, A., Beyersdorf, A., Ziemba, L., Anderson, B., Thornhill,
478 L., Perring, A. E., Schwarz, J. P., Campazano-Jost, P., Day, D. A., Jimenez, J. L., Hair, J. W., Mikoviny, T.,
479 Wisthaler, A., & Sorooshian, A.: Airborne characterization of subsaturated aerosol hygroscopicity and dry refractive
480 index from the surface to 6.5km during the SEAC⁴RS campaign, *J. Geophys. Res.*, 121(8), 4188-4210,
481 <https://doi.org/10.1002/2015JD024498>, 2016.

482 Shinozuka, Y., Saide, P. E., Ferrada, G. A., Burton, S. P., Ferrare, R. A., Doherty, S. J., Gordon, H., Longo, K., Mallet,
483 M., Feng, Y., Wang, Q., Cheng, Y., Dobracki, A., Freitag, S., Howell, S. G., LeBlanc, S., Flynn, C., Segal-
484 Rozenhaimer, M., Pistone, K., Podolske, J. R., Stith, E. J., Bennett, J. R., Carmichael, G. R., da Silva, A.,

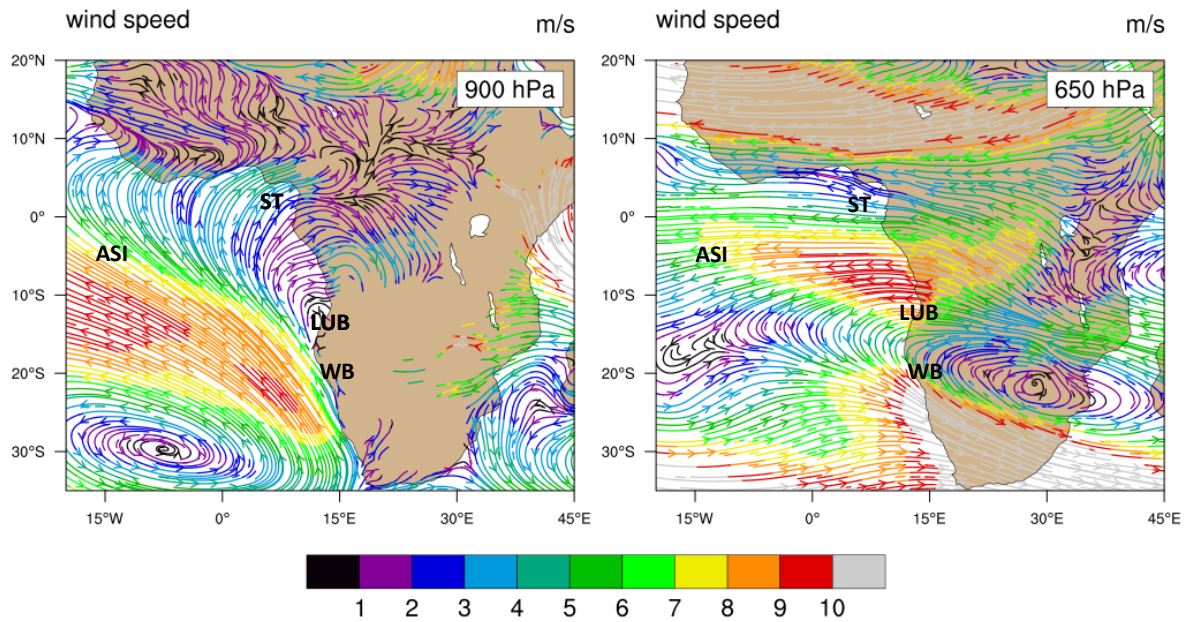
485 Govindaraju, R., Leung, R., Zhang, Y., Pfister, L., Ryoo, J.-M., Redemann, J., Wood, R., and Zuidema, P.: Modeling
 486 of the smoky troposphere of the southeast Atlantic: a comparison to ORACLES airborne observations from
 487 September of 2016, *Atmos. Chem. Phys.*, 20, 11491-11526, doi:10.5194/acp-20-11491-2020, 2020.
 488 Shipley, S. T., Tracy, D. H., Eloranta, E. W., Tauger, J. T., Stroga, J. T., Roesler, F. L., and Weinman, J. A.: High
 489 spectral resolution lidar to measure optical scattering properties of atmospheric aerosols. 1. Theory and
 490 instrumentation, *Appl. Optics*, 22, 3716-3724, 1983.
 491 Stein, A.F., Draxler, R. R., Rolph, G. D., Stunder, B. J. B., Cohen, M. D., and Ngan, F.: NOAA's HYSPLIT
 492 atmospheric transport and dispersion modeling system, *B. Am. Meteorol. Soc.*, 96, 2059-2077, doi:10.1175/BAMS-
 493 D-14-00110.1, 2015.
 494 Veselovskii, I., Kolgotin, A., Grazianov, V., Müller, D., Wandinger, U., and Whiteman, D. N.: Inversion with
 495 regularization for the retrieval of tropospheric aerosol parameters from multi-wavelength lidar sounding, *Appl.*
 496 *Optics*, 41, 3685-3699, 2002.
 497 Wilcox, E. M.: Stratocumulus cloud thickening beneath layers of absorbing smoke aerosol, *Atmos. Chem. Phys.*, 10,
 498 11769-11777, doi:10.5194/acp-10-11769-2010, 2010.
 499 Wilcox, E. M.: Direct and semi-direct radiative forcing of smoke aerosols over clouds, *Atmos. Chem. Phys.*, 12, 139-
 500 149, doi:10.5194/acp-12-139-2012, 2012.
 501 Wu, H., Taylor, J. W., Szpek, K., Langridge, J. M., Williams, P. I., Flynn, M., Allan, J. D., Abel, S. J., Pitt, J., Cotterell,
 502 M. I., Fox, C., Davies, N. W., Haywood, J., and Coe, H.: Vertical variability of the properties of highly aged biomass
 503 burning aerosol transported over the southeast Atlantic during CLARIFY-2017, *Atmos. Chem. Phys.*, 20, 12697-
 504 12719, <https://doi.org/10.5194/acp-20-12697-2020>, 2021.
 505 Xu F., Gao, L., Redemann, J., Flynn C.J., Espinosa, W.R., da Silva, A.M., Starnes, S., Burton, S.P., Liu, X., Ferrare,
 506 R., Cairns, B. and Dubovik, O.: A Combined Lidar-Polarimeter Inversion Approach for Aerosol Remote Sensing
 507 Over Ocean, *Front. Remote Sens*, 2:620871, doi: 10.3389/frsen.2021.620871, 2021.
 508 Yamaguchi T, Feingold, G., Kazil, J., and McComiskey, A.: Stratocumulus to cumulus transition in the presence of
 509 elevated smoke layers. *Geophys. Res. Lett.*, 42: 10478–10485, 2015.
 510 Zhang, J. and Zuidema, P.: The diurnal cycle of the smoky marine boundary layer observed during August in the
 511 remote southeast Atlantic, *Atmos. Chem. Phys.*, 19, 14493–14516, <https://doi.org/10.5194/acp-19-14493-2019>,
 512 2019.
 513 Zhang Z., Meyer, K., Yu, H., Platnick, S., Colarco, P. R., Liu, Z., and Oreopoulos, L.: Shortwave direct radiative
 514 effects of above-cloud aerosols over global oceans derived from 8 years of CALIPSO and MODIS observations,
 515 *Atmos. Chem. Phys.*, 16, 2877-2900, doi:10.5194/acp-16-2877-2016, 2016.
 516 Zhang, X., Mao, M., Yin, Y., and Tang, S.: The absorption Ångström exponent of black carbon with brown coatings:
 517 effects of aerosol microphysics and parameterization, *Atmos. Chem. Phys.*, 20, 9701-9711, doi:10.5194/acp-20-
 518 9701-2020, 2020.
 519 Zuidema, P., Redemann, J., Haywood, J., Wood, R., Piketh, S., Hipondoka, M., and Formenti, P.: Smoke and clouds
 520 above the southeast Atlantic, *B. Am. Meteorol. Soc.*, 97, 1131-1135, doi:10.1175/BAMS-D-15-00082.1, 2016.
 521 Zuidema, P., Sedlacek III, A. J. Flynn, C., Springston, S., Delgado, R., Zhang, J., Aiken, A. C., Koontz, A., and
 522 Muradyan, P.: The Ascension Island boundary layer in the remote Southeast Atlantic is often smoky, *Geophys. Res.*
 523 *Lett.*, 45, 4456-4465, doi:10.1002/2017/GL076926, 2018.
 524

525
526
527

Table 1: Averaging area, flight time periods, the duration over water and number of HYSPLIT backward trajectories, and number of HSRL-2 profiles in each grid box used in the study.

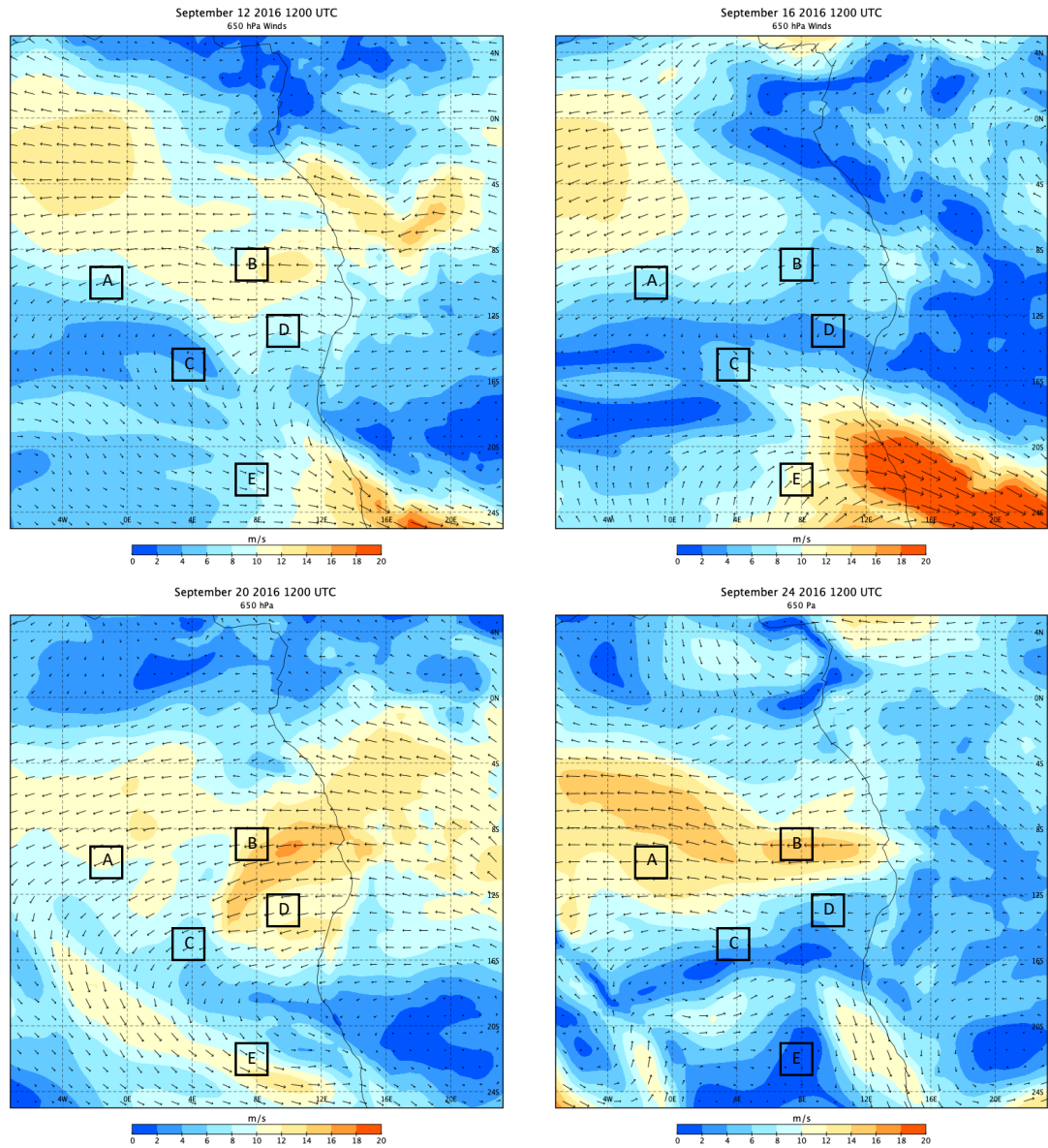
Box	Averaging Area	Averaging Days	Time of Day	Duration in Hours Over Water at 3.5 km	Number of Profiles
A	11° S-9° S; 1° W-1° E	9/12,16	11:00 UTC	44.3±7.0 (N = 19)	50
B	10° S-8° S; 8° E-10° E	9/12,16,18	10:00 UTC	14.9±4.5 (N = 27)	56
C	16° S-14° S; 4° E-6° E	9/12,16	13:00 UTC	40.4±7.2 (N = 19)	51
D	14° S-12° S; 10° E-12° E	9/18,24	09:00 UTC	5.5±2.0 (N = 27)	46
E	23° S-21° S; 8° E-10° E	9/20,22	14:00 UTC	-	36

528



530
 531
 532
 533
 534
 535

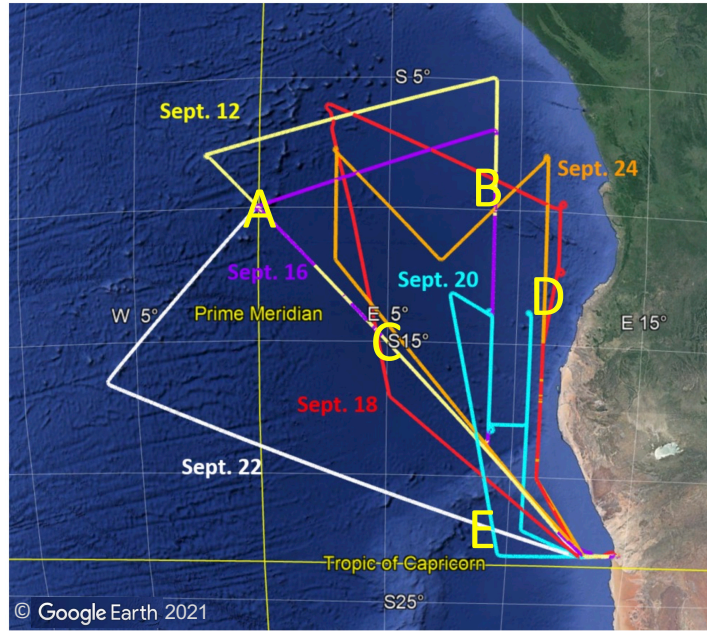
Figure 1: MERRA2 monthly mean reanalysis of 900 and 650 hPa streamlines for September 2016. Stations marked are Ascension Island (ASI), Lubango (LUB), a long-term AERONET site at 2 km elevation, and Walvis Bay (WB), where ER-2 flights originated from during the September 2016 ORACLES IOP. Flights in August 2017 and September/October 2018 originated from São Tomé (ST).



536
537
538
539

Figure 2: MERRA2 reanalysis of 650 hPa winds at 1200 UTC on September 12, 16, 20, 24, 2016. Grid boxes in the study are marked with letters.

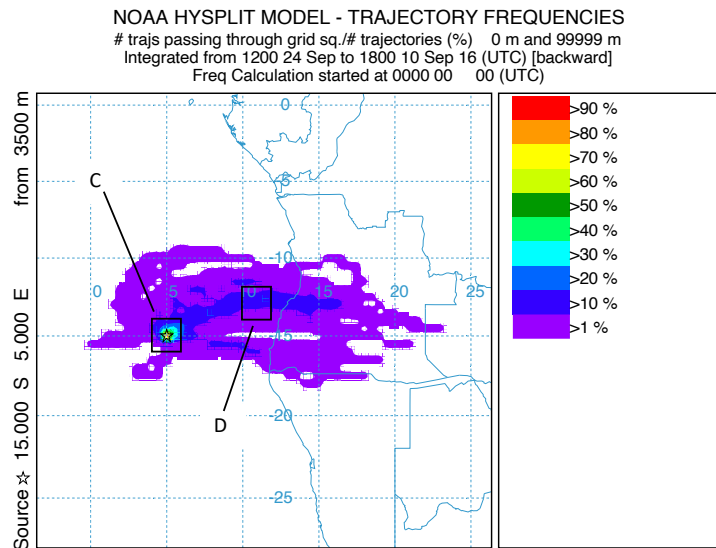
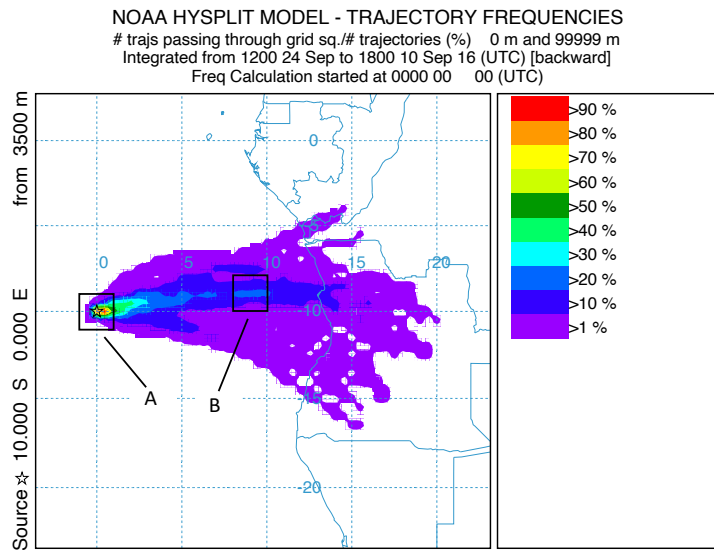
540
541



542
543

544
545
546

Figure 3: HSRL-2 science data flight tracks during the September 2016 IOP. Letters refer. to the grid boxes identified in Fig. 2 (© Google Earth).



548
 549
 550
 551
 552
 553

Figure 4: Frequency distribution of 48-hour backward trajectories of air parcels arriving at 3500 m above the centers of grid boxes A and C over the time period of the campaign. Grid boxes B and D are upstream of grid boxes A and C, respectively.

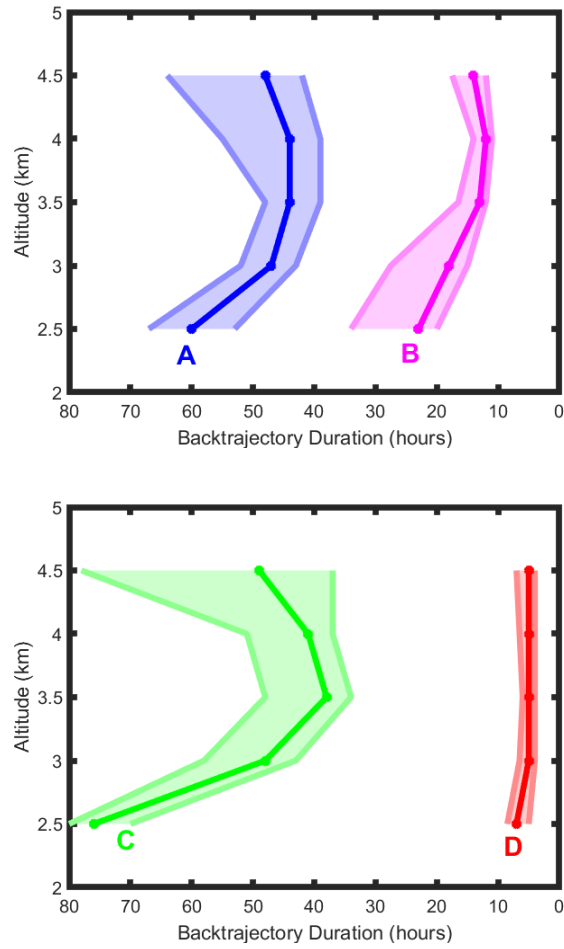
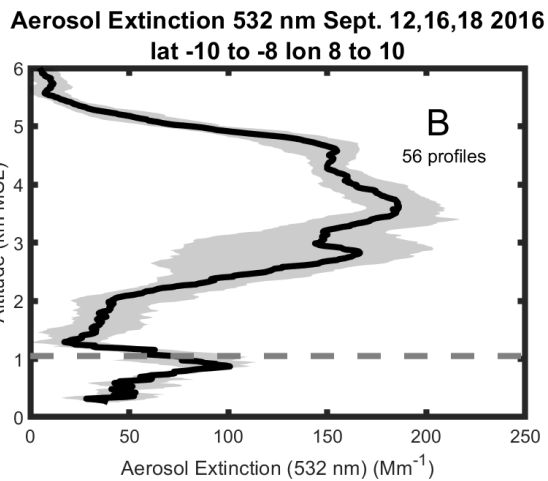
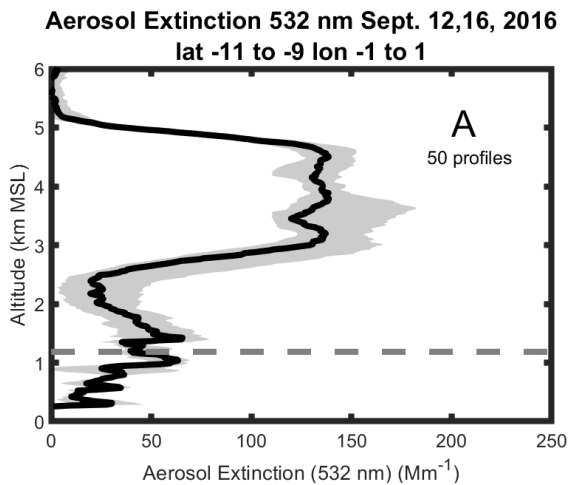


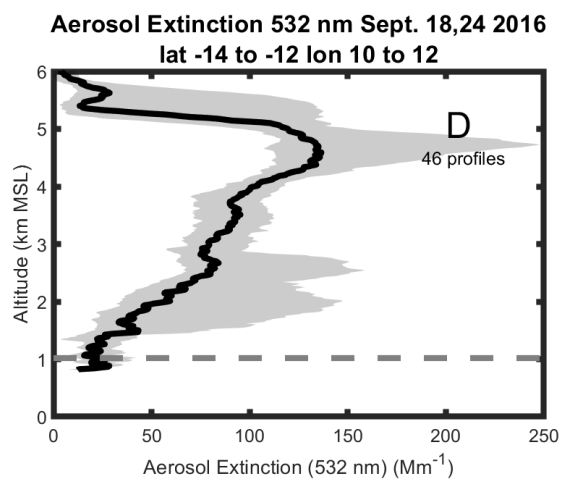
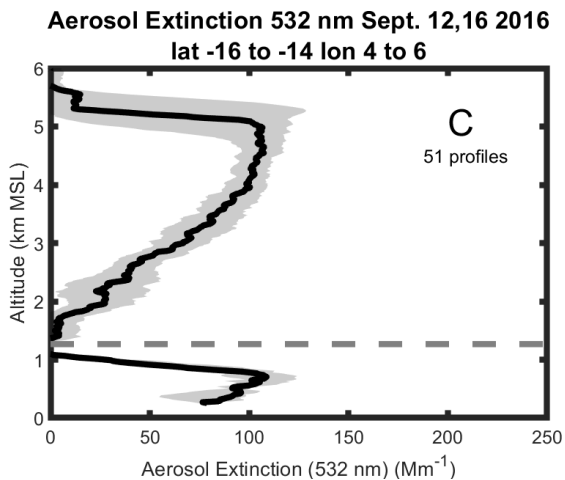
Figure 5: Duration of time spent over water of air parcels arriving at grid boxes marked on the figure. Solid lines are median values, and the shaded portion are the range of the 75th and 25th percentile. The number of trajectories used for the calculation are in Table 1. Trajectory hours are shown in reverse to correspond to the map in Fig. 4.

555
 556
 557
 558
 559
 560
 561

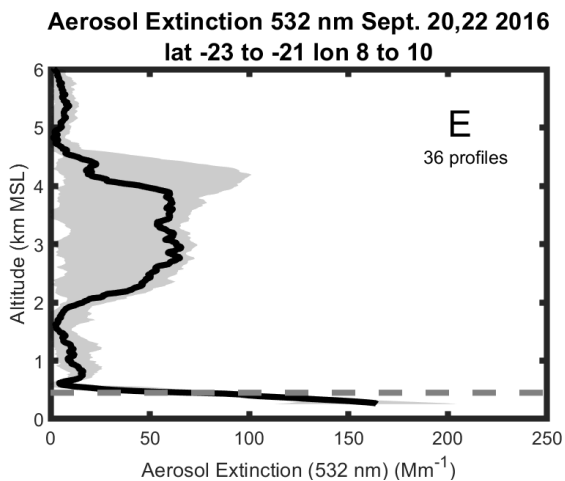
562



563



564

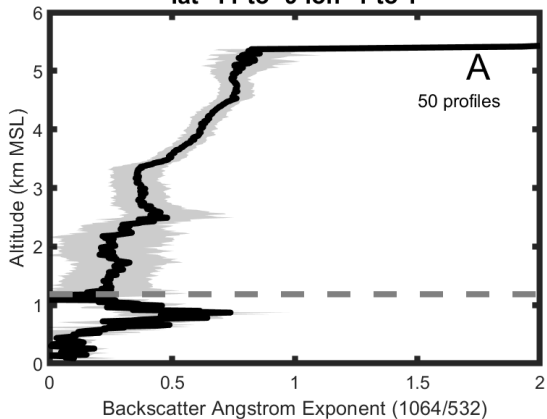


565
566
567
568
569
570
571

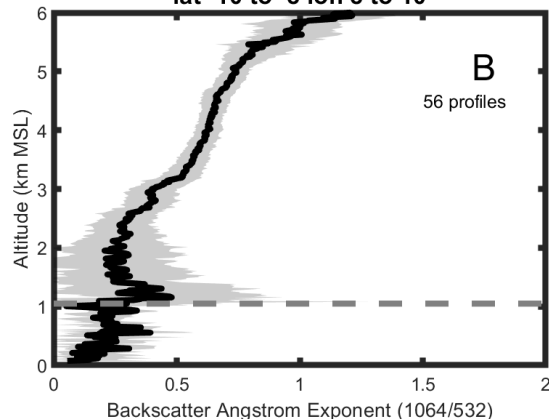
Figure 6: Average vertical profiles of the aerosol extinction coefficient at 532 nm in grid boxes A (upper left), B (upper right), C (middle left), D (middle right) and E (lower left). The averaging area, dates of flights and total number of one-minute profiles are also shown. The dark line represents the median value and grey shades contain the 25th to 75th percentiles. Dashed line refers to the mean cloud top height.

572

Backscatter Ang. Expo. 1064/532 Sept. 12,16, 2016
lat -11 to -9 lon -1 to 1

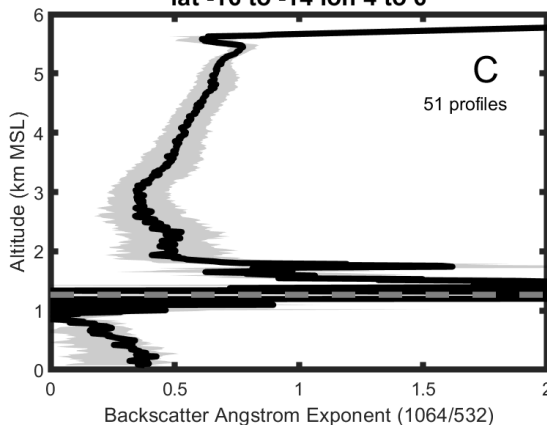


Backscatter Ang. Expo. 1064/532 Sept. 12,16,18 2016
lat -10 to -8 lon 8 to 10

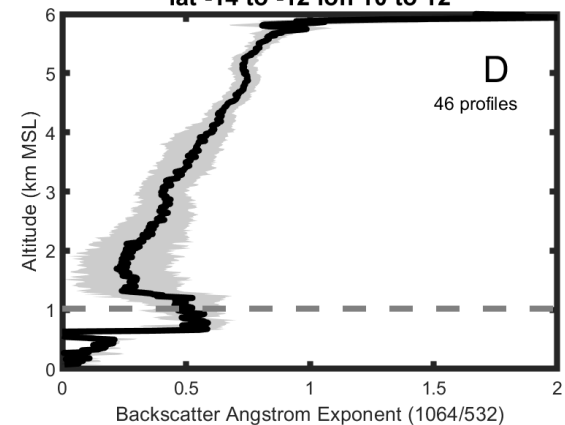


573

Backscatter Ang. Expo. 1064/532 Sept. 12,16 2016
lat -16 to -14 lon 4 to 6

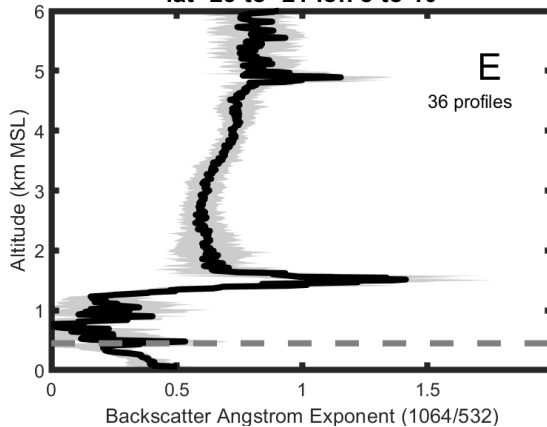


Backscatter Ang. Expo. 1064/532 Sept. 18,24 2016
lat -14 to -12 lon 10 to 12



574

Backscatter Ang. Expo. 1064/532 Sept. 20,22 2016
lat -23 to -21 lon 8 to 10

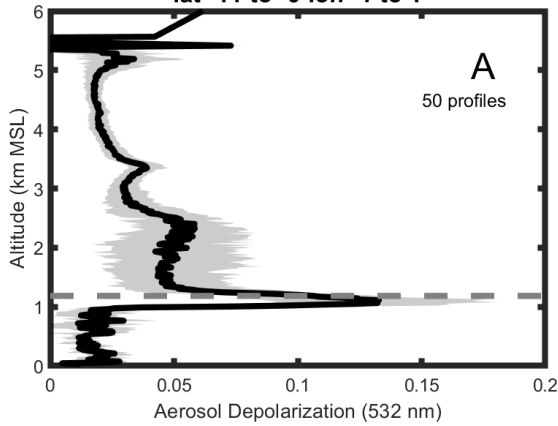


575
576
577
578
579

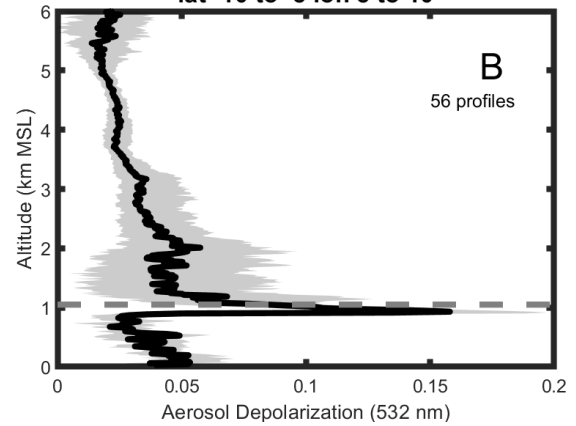
Figure 7: As in Fig. 6 but for the Wavelength Dependent Backscatter Ångström exponent between 1064 and 532 nm.

580

Aerosol Depolarization 532 nm Sept. 12,16, 2016
lat -11 to -9 lon -1 to 1

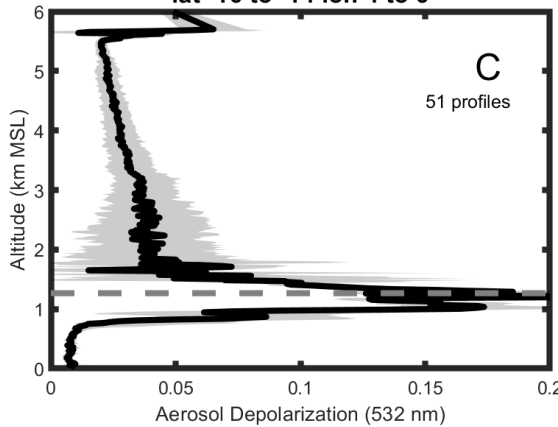


Aerosol Depolarization 532 nm Sept. 12,16,18 2016
lat -10 to -8 lon 8 to 10

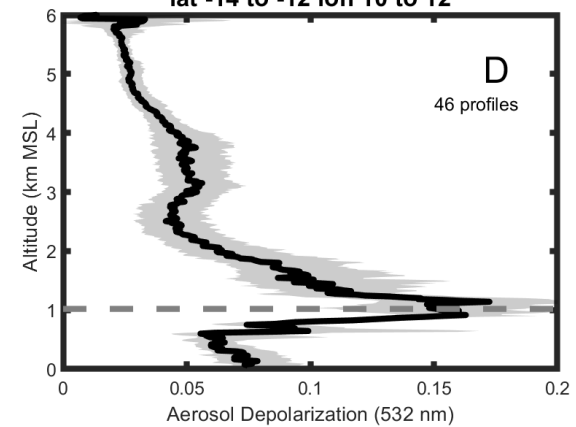


581

Aerosol Depolarization 532 nm Sept. 12,16 2016
lat -16 to -14 lon 4 to 6

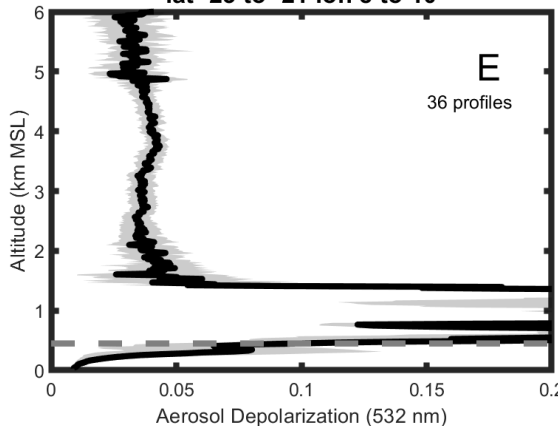


Aerosol Depolarization 532 nm Sept. 18,24 2016
lat -14 to -12 lon 10 to 12



582

Aerosol Depolarization 532 nm Sept. 20,22 2016
lat -23 to -21 lon 8 to 10



583

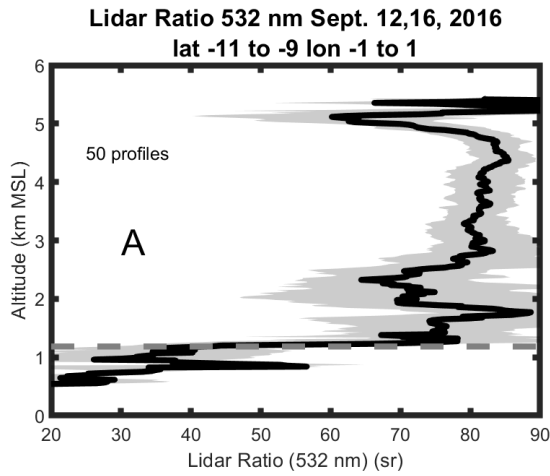
584

585

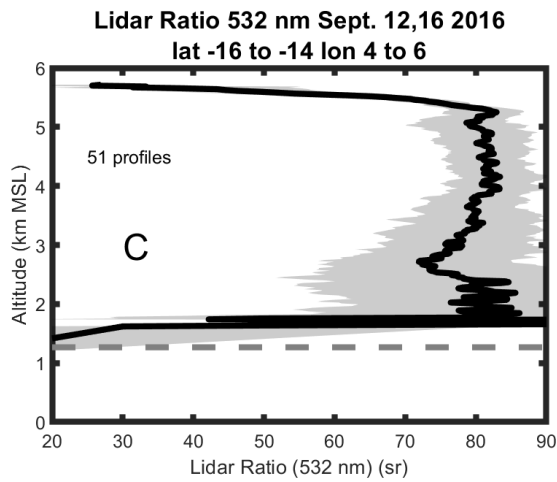
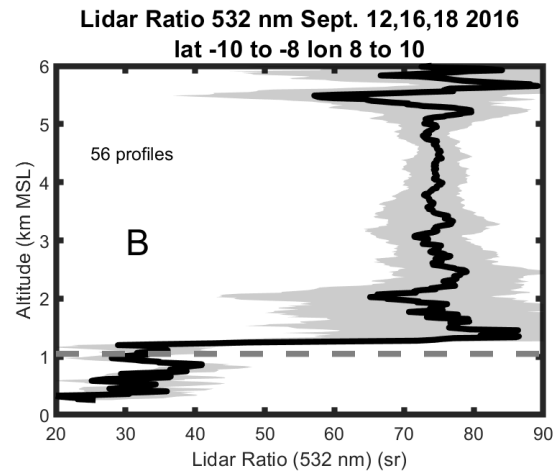
586

Figure 8: As in Fig. 6 but for the aerosol depolarization at 532 nm.

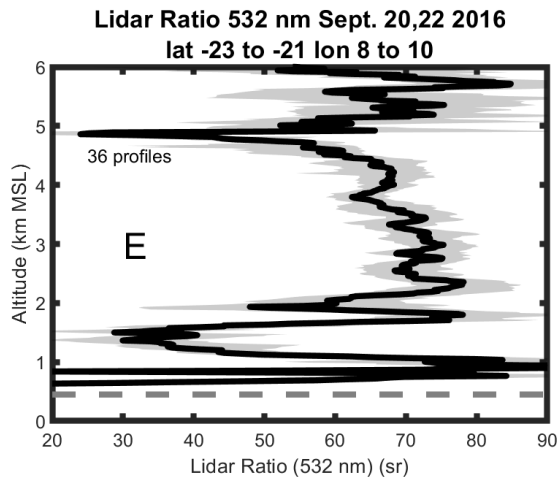
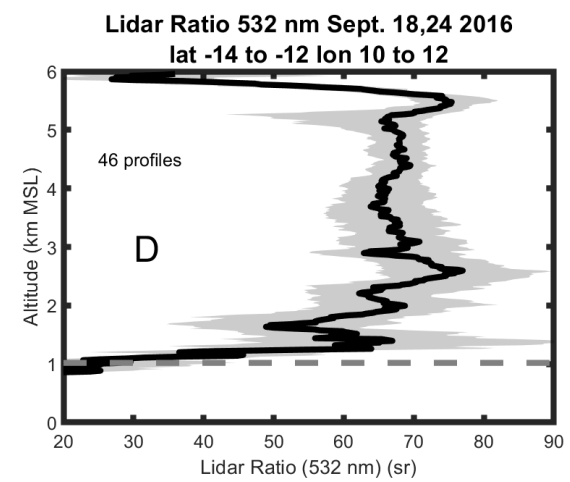
587



588

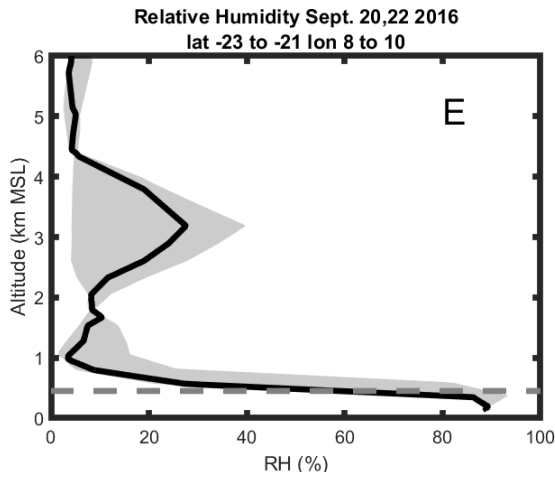
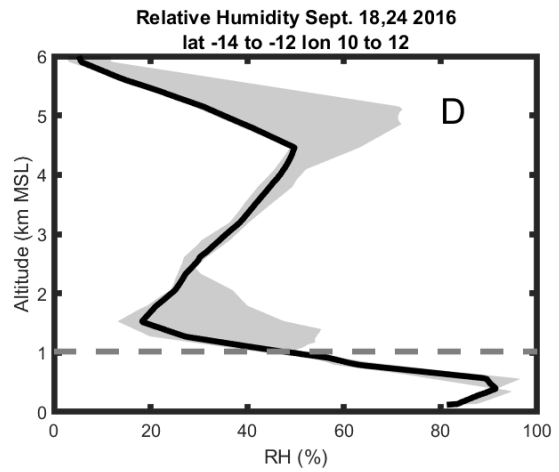
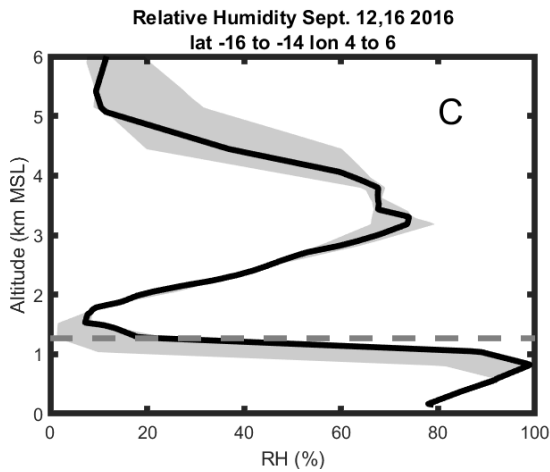
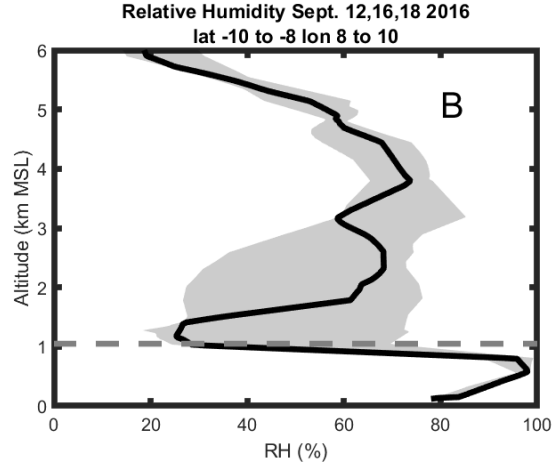
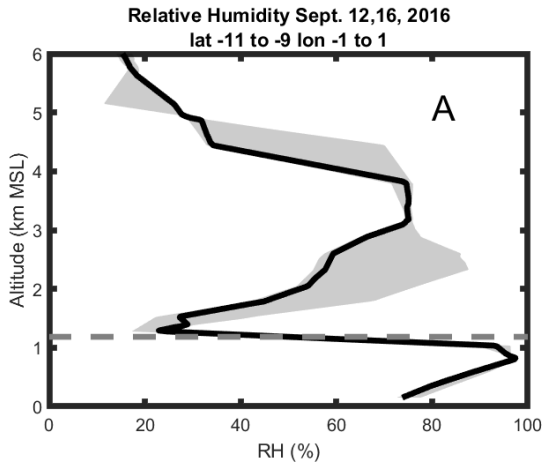


589



590
591
592
593

Figure 9: As in Fig. 6 but for the Lidar Ratio at 532 nm.



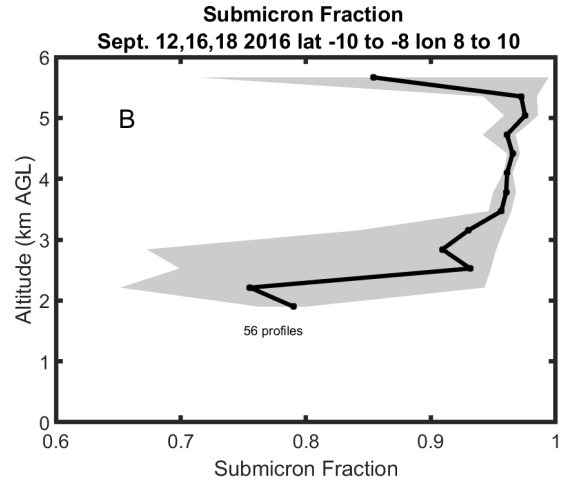
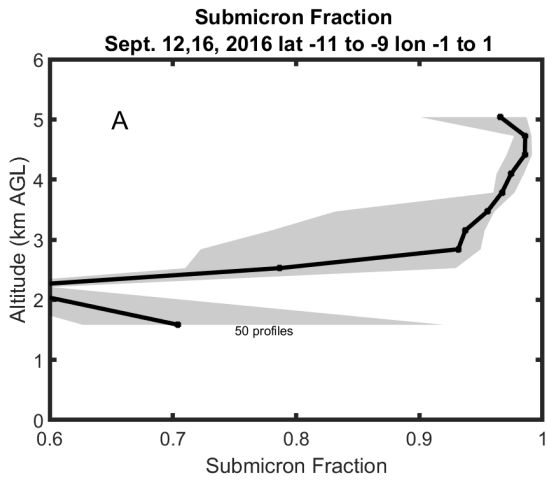
594

595

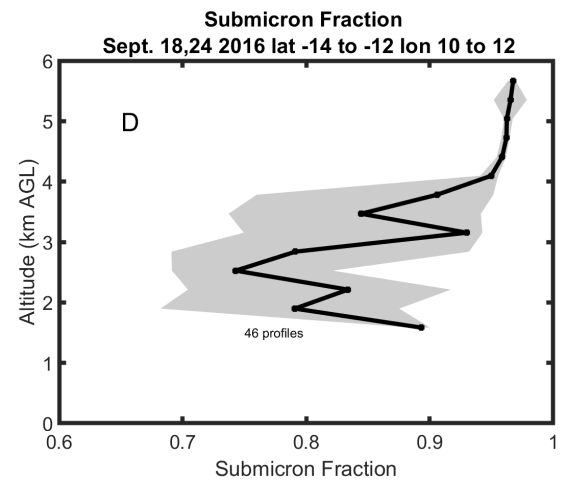
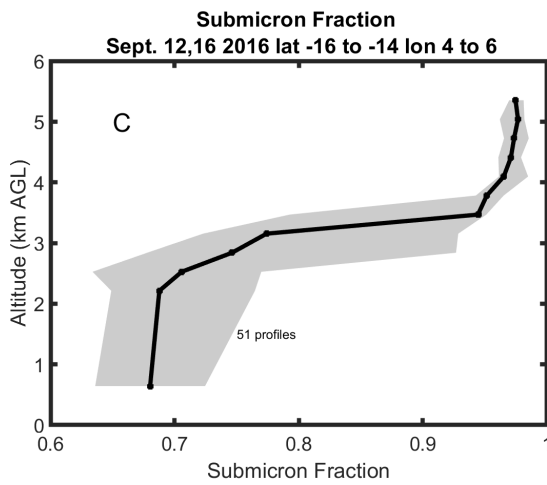
596
597
598
599
600
601
602
603

Figure 10: Relative Humidity (%) in grid boxes A (upper left), B (upper right), C (middle left), D (middle right) and E (lower left) from MERRA2 reanalysis corresponding to the HSRL-2 profiles shown in Figs. 6-9. The dark line represents the median value and grey shades contain the 25th to 75th percentiles. Dashed line refers to the mean cloud top height.

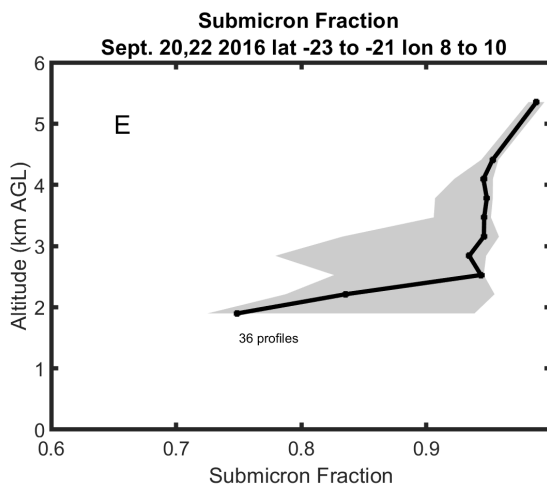
604



605



606



607

608

609

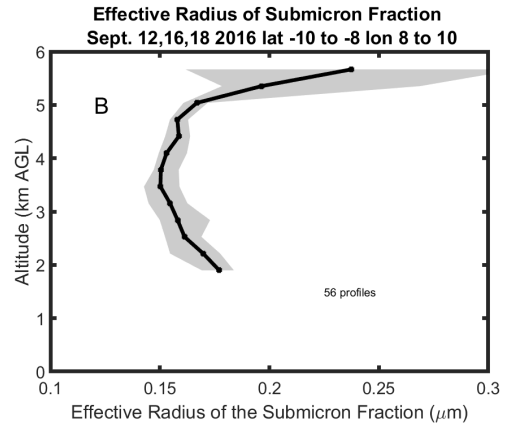
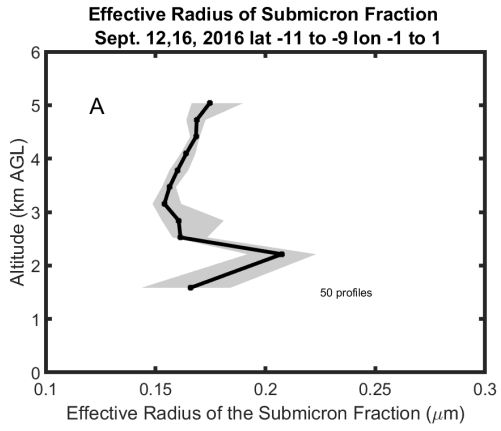
610

611

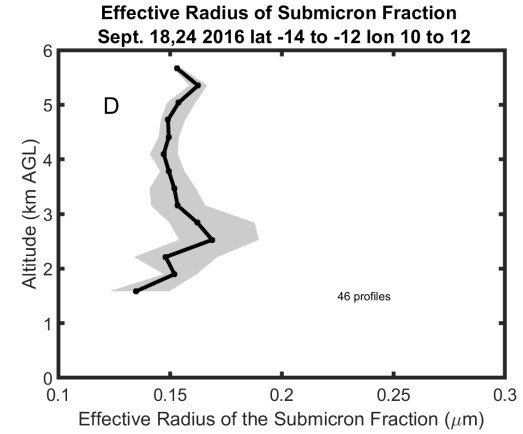
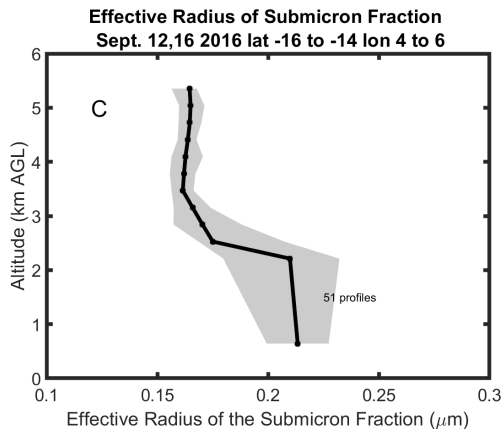
612

Figure 11: Average vertical profiles of the submicron fraction in grid boxes A (upper left), B (upper right), C (middle left), D (middle right) and E (lower left). The averaging area, dates of flights and total number of one-minute profiles in the average are also shown. The dark line represents the median value and grey shades contain the 25th to 75th percentiles.

613



614



615

616

617

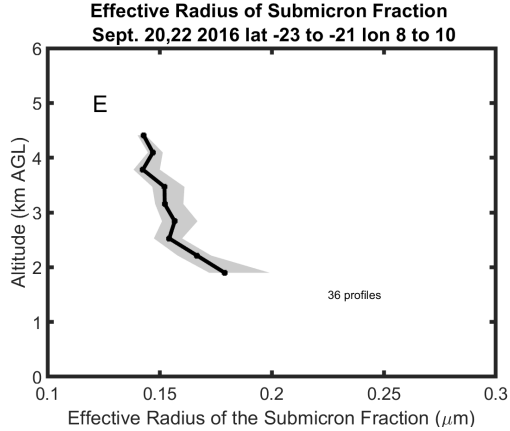


Figure 12: As in Fig. 11 but for the effective radius of the submicron fraction.